Flow over a Wing with Leading-Edge Undulations

Alex Skillen, Alistair Revell, Alfredo Pinelli, Ugo Piomelli, Julien Favier

Flow over a Wing with Leading-Edge Undulations

A Skillen[1], A Revell[1], A Pinelli[2], U Piomelli[3], J Favier[4]

[1]*Modelling and Simulation Centre, School of MACE, The University of Manchester, UK*

[2]*School of Engineering and Mathematical Science, City University London, UK*

[3]*Dept. of Mechanical and Materials Engineering, Queen's University,*

Kingston (Ontario) K7L 3N6, Canada.

[4]*Aix Marseille Université, CNRS, Centrale Marseille, M2P2 UMR 7340, 13451, Marseille, France.*

The stall-delaying properties of the humpback whale flipper have been observed and quantified in recent years, through both experimental and numerical studies. In the present work we report numerical simulations of an infinite span wing with an idealised representation of this geometry, at a Reynolds number of 1.2×10^5. Using Large Eddy Simulation, we first establish an adequate spatial resolution before also examining the spanwise extent of the domain. We then proceed to analyse these results to provide an explanation of the conditions that drive the lift observed beyond the conventional stall angle. The undulating leading-edge geometry gives rise to a span-wise pressure gradient that drives a secondary flow towards the regions of minimum chord. In turn, this leads to the entrainment of higher-momentum fluid into the region behind the maximum chord, which energises the boundary layer and delays stall. Aside from demonstrating a significant post-stall lift, the undulations also have the added benefit of substantially reducing lift fluctuations.

Introduction

For some time now it has been observed that the humpback whale *(Megaptera novaeangliae)* is highly maneuverable and, despite its large size, is able to execute tight under-water rolls and loops when pursuing prey. In view of this fact, Fish and Battle [1] undertook a detailed study to understand better the morphology of the whale's flipper. They were amongst the first to elaborate on the hydrodynamic significance of protuberances (or undulations) that can be seen along the leading edge of the flipper. It was suggested that they may act as a passive flow-control device, delaying the stall angle. A proposed mechanism similar to that of vortex generators or strakes was suggested, whereby the boundary-layer is re-energised by momentum transfer from the freestream.

After this early morphological investigation, several studies attempted to demonstrate the feasibility of leading-edge undulations as passive flow control devices for wings, to quantify the magnitude of any benefit that they may offer. Miklosovic et al. [2] performed wind-tunnel measurements on an idealised flipper model, both with and without undulations. They reported a delay in the stall angle of around 40%, with higher post-stall lift and lower post-stall drag. Johari et al. [3] performed an experimental study on *infinite* or quasi-two-dimensional wings (i.e. where wing-tip effects are eliminated) with sinusoidal undulations covering a range of amplitudes and wavelengths. The authors observed a slight reduction in pre-stall aerodynamic performance, but noted that in the post-stall regime, the lift was up to 50% higher than the baseline case without undulations. Similar findings were later reported by Hansen et al. [4], in which wind tunnel measurements were conducted on various undulating geometries. They observed significant performance enhancement across a broad range of geometric parameters. Significantly, the eventual stall of the undulating wing was gradual, as opposed to the baseline unmodified wing in which a dramatic and sudden loss in lift is experienced at stall.

Several attempts have been made to elucidate the physical mechanisms by which the undulations offer their benefit. Miklosovic et al. [5] experimentally investigated the effect of undulations on the formation of wing-tip vortices by comparing a quasi-two-dimensional configuration against

a fully three-dimensional one. The study was motivated by the hypothesis that the undulations may gain their performance benefit by increasing the effective span of a finite wing by diminishing the spanwise flow component, thereby reducing the losses associated with the wing-tip vortex. In their preliminary findings, the authors observed a significant performance decrease for the quasi-2D model relative to their 3D one, leading to the proposal that the wing-tip effect is indeed significant. It must be noted, however, that the operating Reynolds number for the full-span case was less than half that of the finite span. Stanway [6] later performed PIV measurements around a finite wing with protuberances, in which a strong sensitivity of the performance enhancement to the flow Reynolds number was observed, thereby casting doubt over the proposed significance of the wing-tip vortices. Finally, Hansen et al. [4], demonstrated that both three-dimensional and quasi-two-dimensional configurations offered similar qualitative characteristics in the lift curve, further indicating that the wing tip effect is not as significant as originally thought.

The hypothesis that the undulations may act in a similar way to vortex generators was advanced by Miklosovic et al. [2], Fish and Lauder [7], Fish et al. [8], and Zhang et al. [9]. However, van Nierop et al. [10] point out that, since the wavelength and amplitude of the undulations is significantly greater than the boundary layer thickness, the mechanism must be different from that of conventional vortex generators as defined in e.g. [11]. The authors of [10] go on to develop an analytical model (with empirical inputs) of the undulating wing, and propose a mechanism whereby separation is delayed behind chord peaks due to a non-uniform downwash, which reduces the effective angle of attack behind the peaks. Further, the authors observe that since the chord length is lower behind a trough (compared with the peaks), the streamwise pressure gradient must be greater there. Separation is therefore initiated in the region behind the troughs, and the flow in the regions behind the peaks remain attached for longer distances.

There have been a number of attempts at modelling this flow numerically. One of the first such efforts was conducted by [12] using a panel method. However, due to the inviscid approximation inherent in the panel method, flow separation cannot be predicted, and little light could be shed on

the complex flow physics. Yoon et al. [13] conducted a computational study of a low aspect-ratio wing with varying coverage by the undulations (i.e. a portion of the leading edge close to the root was left straight). They employed a steady-state CFD solver, and used a Reynolds-averaged turbulence closure ($k-\omega$ SST). The authors observed that, as a greater portion of the wing's leading edge was covered with undulations, the stall angle was lowered. However, under post stall conditions, the lift had recovered, and increased coverage by the undulations ultimately led to increased performance. Recently, Xingwei et al. [14] performed a Reynolds-averaged study of wings with a sinusoidal leading edge during forward flapping and gliding flight. Webber et al. [15] performed a study of the flow over a full flipper, again with Reynolds-averaged turbulence closure (Spalart–Allmaras was compared against $k-\omega$). The authors report severe inaccuracy in the post-stall regime, thereby raising questions about the suitability of either one or two-equation Reynolds-averaged closure to this problem. This question is particularly significant if secondary flow features are indeed central to the flow enhancement, as indicated in the present work. Pedro and Kobayashi [16] carried out Detached Eddy Simulations (DES) of a similar configuration and found reasonable agreement with experiments in terms of integral quantities.

Favier et al. [17] conducted direct numerical simulations of an undulating geometry at low Reynolds number. A parametric study was performed on the undulation's geometric parameters, covering a range of wavelengths and amplitudes. While the authors observed a peak drag reduction of 35%, the lift was also reduced relative to the baseline unmodified case for all configurations. This result is likely to be a consequence of the low flow Reynolds number considered (several orders of magnitude lower than that observed in nature, and lower than that required for transition to turbulence). In the study, a Kelvin-Helmholtz-like instability, driven by the spanwise modulation of the streamwise velocity component by the undulations, was identified. It was reasoned that this instability generates rolls of vorticity emanating from the undulation site. The rolls, initially vertical, are tilted into the streamwise direction. The vortices increase aerodynamic performance by acting on boundary-layer separation and promoting attachment.

While some insight has been gained into the principal flow mechanisms, a detailed flow physics investigation has not been provided thus far, especially under turbulent conditions. Specifically, while the performance benefit has been quantified in terms of the integral quantities for a range of different wavelengths and undulation amplitudes [4], the effect of these parameters on the flow physics is unclear. While it is generally accepted that the undulations induce a vortex system, the mechanisms responsible for the generation of those large scale vortical structures is unclear. Probably, different physical mechanisms contribute to the post-stall flow modification, and the dominance of each single effect depends on the geometrical configuration and flow Reynolds number.

The aim of the present study is to take a step towards a deeper understanding of a mechanism that can bring significant aerodynamic benefits. By exploring the flow-physics for a single configuration with an unprecedented level of detail, we have uncovered a flow mechanism that may be responsible for the performance gain reported in a number of studies. The present study is carried out via highly-resolved Large Eddy Simulations (LES) of the flow, both with and without sinusoidal leading-edge undulations. In both cases, the flow Reynolds number based on mean chord length and bulk velocity is $120,000$, and the incidence angle is 20°. An improved understanding of the flow under these conditions is expected to be of direct relevance to the Unmanned Air Vehicle (UAV) industry, as well as for wind turbines and fans, all of which operate at a similar Reynolds number. In addition, studies of this nature provide an important benchmark for the assessment of more industrial turbulence modelling approaches, which may then be used to extend the parameter space to higher Reynolds number.

In the following, we will first describe the numerical model. Then, after validating the results by comparison to data in the literature, we discuss the physical mechanisms that characterise the behavior of the wing at high angle-of-attack. This is followed by conclusions and recommendations for future work.

Numerical approach

The filtered incompressible Navier-Stokes equations govern the flow dynamics:

$$\begin{aligned} &\frac{\partial \overline{u}_i}{\partial t} + \frac{\partial}{\partial x_j}\left(\overline{u}_i \overline{u}_j\right) = \\ &\quad \frac{\partial}{\partial x_j}\left[-\frac{\overline{p}}{\rho}\delta_{ij} + \nu\left(\frac{\partial \overline{u}_i}{\partial x_j} + \frac{\partial \overline{u}_j}{\partial x_i}\right) - \tau_{ij}\right] \\ &\frac{\partial \overline{u}_i}{\partial x_i} = 0 \end{aligned} \tag{1}$$

where an overbar denotes a filtered variable, and τ_{ij} is the residual stress tensor. The filtering operation is performed implicitly by the mesh.

Equations 1 are closed via an eddy viscosity model [18];

$$\tau_{ij} = -2c_s\Delta^2 \left|\overline{S}\right| \overline{S}_{ij} \tag{2}$$

where $\overline{S}_{ij}$ is the resolved strain rate tensor, $\left|\overline{S}\right| = \sqrt{2\overline{S}_{ij}\overline{S}_{ij}}$, and Δ is the local filter width, taken as $V^{1/3}$ (where V is the cell volume). The model constant $c_s(\mathbf{x}, t)$ is set dynamically according to the Germano-Lilly procedure [19, 20]. For further information on LES for incompressible flows, the reader is referred to [21].

The governing equations are discretised via the finite volume method. The space discretisation is based on a second-order accurate central finite volume method. The equations are advanced in time via a second-order semi-implicit method, by treating the advective terms with an Adams-Bashforth scheme and the viscous ones through the implicit Crank-Nicholson method. The time-step size is set to yield a maximum global Courant number around 0.6. Pressure-velocity coupling is achieved via the PISO algorithm [22].

The discretised equations are advanced in time using the OpenFOAM package until first and

second order statistics are fully converged. After the initial transient, data gathered over 400 dimensionless time units (defined as $t' \equiv Ut/\overline{c}$, where U is the bulk velocity, t and t' are the physical and dimensionless times respectively, and $\overline{c}$ is the mean chord) is sufficient to attain converged statistical quantities.

Geometry and mesh

Figure 1 shows the characteristic undulating leading-edge wing geometry considered in this study. A NACA 0021 wing section is employed and is set at an angle of attack of 20°; a post-stall condition. The chord length for the undulating cases varies as:

$$c(z) = A\cos\left(\frac{2\pi z}{\lambda}\right) + \overline{c} \tag{3}$$

where A is the amplitude of the undulation, λ is the wavelength of the undulation, and z is the spanwise ordinate. For the case considered here, we use $A = 0.015\overline{c}$ and $\lambda = 0.11\overline{c}$, corresponding to a case considered experimentally in [4]. The flow over the baseline unmodified NACA 0021 profile is also computed for comparison.

Meshes comprising around 3.5×10^7 cells have been used, with around $150,000$ cells in each xy-plane. All meshes are of block-structured hexahedral topology, with a 'C-shape' grid being wrapped around the wing. The same mesh density in the xy-plane is employed throughout the span, with the mesh being smoothly adjusted to conform to the contour of the geometry at the undulation site. Near-wall cells are placed at $y^+ < 1$ everywhere, with the grid stretching in the wall normal direction not exceeding 5%. Figure 2 shows the grid spacing in wall units for the undulating geometry behind both the chord maxima and minima, from which it is apparent that the present LES is very well resolved near the wall.

The computational domain reaches $10\overline{c}$ upstream of the leading edge, and $15\overline{c}$ downstream of the trailing edge. Lateral boundaries are placed $15\overline{c}$ from the wing, while the spanwise extent is set to $0.44\overline{c}$ (corresponding to four wavelengths of the undulation). We compute the two-point

correlation (defined as $R_{ij}(\mathbf{x}, \mathbf{r}) \equiv \langle u_i(\mathbf{x}) u_j(\mathbf{x}+\mathbf{r}) \rangle / (\langle u_i(\mathbf{x}) u_j(\mathbf{x}) \rangle)$) between a point at $\mathbf{x}$, and a second point displaced by $\mathbf{r}$ from $\mathbf{x}$ (where $\mathbf{r}$ is a vector pointing in the spanwise direction). Several locations $\mathbf{x}$ in the separated shear layer and recirculation region have been considered; a representative selection of which are presented in Figures 3 and 4 for the modified and unmodified geometries respectively.

The two-point correlation becomes small for $r/c > 0.22$ (half of the domain width) in all cases except for point 4, where it remains significant. This is due to the presence of large, coherent, spanwise-orientated vortices that are created in the separation region and periodically shed. One such vortex is shown, for the unmodified geometry, in Figure 5. It can be seen that its scale is much larger than that of the turbulence. The inset shows contours of spanwise vorticity near the vortex in an xy-plane. The positive spanwise vorticity corresponds to the counter-rotating motion generated in the recirculation zone.

To ensure sufficient extent in the periodic spanwise direction, tests with a reduced span (half of the original one) were conducted. Similar turbulent shear stress profiles (Fig. 6), and almost indistinguishable mean velocity profiles (Figure 7) were obtained from the two domain sizes. For the unmodified geometry, the difference in mean force coefficients between the two domain sizes were less than 0.5% , while for the modified geometry, there was no measurable difference in mean force coefficients. All subsequent results presented herein have been obtained with the larger span (4λ).

Boundary conditions

A uniform velocity is applied at the inlet, with zero free-stream turbulence. Lateral boundaries are modelled as slip walls. At the outlet, a zero pressure condition is employed, while periodicity is applied in the spanwise direction. The wing surface is modelled as a non-slip wall with zero surface-velocity and a zero gradient condition in the wall-normal direction for the surface pressure. No special treatment is required at the wall since the grid is sufficiently fine to resolve

Table 1. Mean lift and drag coefficients

	$\langle C_l \rangle$	$\langle C_d \rangle$
Baseline geometry		
Ref. [23], $Re = 83,200$	~ 0.56	–
Ref. [23], $Re = 176,000$	~ 0.78	–
Ref. [4], $Re = 120,000$	~ 0.54	~ 0.31
Present study, $Re = 120,000$	0.64	0.32
Modified geometry		
Ref. [4], $Re = 120,000$	~ 0.72	~ 0.28
Present study, $Re = 120,000$	1.03	0.13

fully the boundary layer, and the dynamic sub-grid model gives the correct asymptotic behaviour approaching a solid surface without the need for damping functions. [19].

Results

A. Comparison against experimental data

Presented in Table 1 and Figure 8 are experimental values of the integral quantities (lift and drag coefficients) from comparable experimental studies available in the literature. The baseline lift coefficient obtained in the present study lies well within the range indicated in [23] at two different Reynolds numbers (one above, one below). Assuming a linear variation in the lift at fixed incidence between the two available bounding Reynolds numbers ($Re = 83,200$ and $Re = 176,000$), a value $C_l \approx 0.65$ may be expected at $Re = 120,000$. This is in good agreement with the present value of 0.64. Agreement with the baseline lift coefficient obtained in [4] was less satisfactory, showing a $\sim$ 15% discrepancy. The difference between the results of [4] and [23] for this case indicates a strong sensitivity of the stall angle to external conditions. The authors of [4] point out that the increasing lift slope observed in Figure 8 could be due to the presence of a laminar separation bubble, which acts to increase the effective camber of the wing. The same feature is a potential cause of the early stall relative to [23].

One key difference in the conditions of [4] relative to the present study lies in the free-stream turbulence levels. In [4], a free-stream turbulence intensity of $\sim 0.8\%$ is reported, while in our case it is laminar. Blockage effects by the lateral and transverse boundaries are also different; however, preliminary studies conducted over a smaller domain (not presented), suggest the effect is likely to be small. Further work is required in order to determine the cause of any discrepancies.

B. Aerodynamic performance

Figure 9 shows the time history of lift and drag coefficient for both the undulating and baseline cases. The undulating geometry offers a significant gain in the performance of the wing relative to the baseline. It is is clear that the undulating modifications act to remove much of the unsteadiness from the flow, since the variance in the force coefficients is reduced. This result is particularly important for applications where noise suppression is desired.

From the instantaneous lift, we proceed to compute its power spectra, shown in Figure 10. The output frequency is scaled by the bulk velocity and mean chord giving a Strouhal number, $St = f\overline{c}/U_\infty$. We note that, for the unmodified case, there is a dominant frequency at $St \approx 0.6$. If this is scaled by the projected chord in the streamwise direction ($\overline{c} \cdot \sin(\alpha)$) rather than $\overline{c}$, the resulting Strouhal number is approximately 0.21, typical of bluff-body vortex shedding.

For the modified geometry, a broadband peak is observed, from $St \approx 0.4$, and tapering off around the frequency of the second harmonic for the unmodified case. This suggests the vortex shedding is made less coherent; it occupies a band of frequencies rather than being monochromatic. This lack of synchronisation in the shedding leads to the lower amplitude of fluctuations observed in Figure 9.

Figure 11 shows an iso-surface of zero mean streamwise velocity, which is indicative of the size of the separated region. The unmodified case is also presented for comparison. It is apparent from the figure that the size of the recirculation region for the undulating case is dramatically reduced, and that separation is delayed relative to the unmodified geometry. It can also be seen from the

figure that the flow separation is delayed behind peaks to a greater extent than behind the valleys. This is in qualitative agreement with earlier findings in the literature [4, 10]. The reduced size of the separation region explains the improved aerodynamic performance.

C. Physical mechanism behind performance gain

The undulations promote new physical mechanisms, responsible for the reduction and stabilisation of the recirculation region, and thus the performance enhancement. Initially the oncoming flow is deflected by the leading-edge geometry such that the bulk of the flow is redirected behind the chord minima (see Figure 12). This deflection leads to a strong acceleration behind the minima, and consequently forms an enhanced suction peak (relative to the region behind the maxima). The resulting span-wise pressure gradient is apparent from both Figures 12 and 13. Low inertia near-wall fluid is drawn towards the suction peak, resulting in the formation of secondary flow, shown in Figure 14 (here streamlines are regenerated relative to Figure 12 to highlight the secondary flow); significantly, the low-inertia boundary-layer fluid that is transported away by this secondary flow is replaced by higher momentum fluid, drawn from above. This re-energises the boundary-layer behind each chord peak, delaying separation. The re-energisation of the boundary-layer is apparent from plots of the skin friction coefficient, $C_f \equiv \tau_w/(0.5\rho U_\infty^2)$ (Figure 15) which show high shear stress (relative to the unmodified geometry) over an extended region behind the chord peak.

For the region behind the chord minima, flow separation initially occurs close to the leading edge (see e.g. Figure 15, where separation is apparent from the negative skin friction at $x/\overline{c} \approx 0.02$ behind the trough). This is a consequence of the strong adverse pressure gradient there, which in turn is caused by the combination of the aforementioned suction peak, and the reduced local chord length. However, due to the large local velocity gradients in this region, turbulent production is high (see Figure 16) and flow instabilities that lead to the onset of transition to turbulence occur in the separated shear-layer (apparent from plots of turbulent kinetic energy – Fig. 17, and from iso-surfaces of the second invariant of the velocity gradient tensor – Fig. 18). The resulting momentum

transfer due to the turbulent mixing causes this separated shear layer to reattach at $x/\overline{c} \approx 0.12$ behind the trough, at which point the flow bifurcates into a small laminar separation bubble, and a *newly energised boundary layer* upstream and downstream of the reattachment point respectively. Of key significance here is that the boundary-layer is re-energised across the span, but by different mechanisms, and to differing extents, at different spanwise locations – by a secondary flow behind the peaks, and by turbulent mixing behind the troughs.

It can be seen from Figure 18 that for the modified geometry, flow instabilities occur a short distance behind each trough, while laminar flow persists further downstream behind the peaks. This is a result of the elevated turbulence production behind the trough, and a reduction in the production term behind the peaks (See Figure 16). The strong spanwise variance in the strength of the production term is a direct consequence of a large variance in the local velocity gradients, which ultimately arise due to the aforementioned flow deflection by the geometry, resulting in a non-uniform flow acceleration across the span. Slices of streamwise vorticity plotted in Figure 19 provide insight into the locality of these large spanwise gradients and indicate the rate at which the vorticity generated close to the wall spreads across the entire span, feeding into the separated flow region. Figure 19 shows evidence of streamwise vortices that inject high momentum fluid from above into the boundary layer behind the peaks.

An overview of the suction-side surface-flow is provided by Figure 20 which shows the time-averaged wall shear-stress lines. A sketch is also provided, indicating the flow direction, in addition to separation and reattachment lines. The main separation line (i.e. not that of the small laminar separation bubble), displays strong spanwise variance in its streamwise ordinate. This is partially a consequence of the flow behind the chord maxima benefiting from the re-energisation by the secondary flow, as well as the subsequent re-energisation due to transition. Conversely, for the region behind the minima, only the latter mechanism is active. In addition, the relative strength of these re-energisation mechanisms is not the same. Consequently separation is further delayed behind the chord maxima relative to the minima. Shear flow along this separation line generates

a large vortex system, which in turn induces a complex 3D flow field. The vortices transport momentum in the spanwise direction, thereby regulating the shape of the separation region across the span (though their strength is fairly weak, so this effect is small).

Conclusion

Highly resolved LES simulations are presented for the flow over a NACA 0021 wing with leading edge undulations. An undulation amplitude of 1.5% chord and a wavelength of 11% chord has been considered. For this case, a 58% increase in mean lift and a 59% decrease in mean drag is observed, relative to the baseline geometry. The improved performance is due to a reduction in the size of the separated flow zone (relative to that of the standard NACA 0021 wing), thereby yielding a superior aerodynamic form. A reduction in the variance of the force coefficients is also observed for the modified geometry, which is important for applications where acoustic noise is to be minimised.

The mechanisms by which the size of the separation zone is reduced have been explored. The undulations induce a strong spanwise pressure gradient, which leads to the formation of a secondary flow. Low-inertia, near-wall fluid is transported away by the secondary flow, while high momentum fluid is drawn from above, ultimately leading to re-energisation of the boundary layer behind the chord peaks and a delay in flow separation. Additionally, strong flow acceleration between undulation peaks augments turbulence levels, with the enhanced turbulent transfer of momentum further re-energising the boundary layer.

The relative strength of these re-energisation mechanisms (turbulent momentum transfer versus the transfer of momentum by the secondary flow) must be a function of the geometric parameters of the undulation, as well as the flow Reynolds number; in the limit of zero undulation amplitude or infinite wavelength, there is no secondary flow since the geometry reduces to the baseline case. In this limit, the only active mechanism could be the turbulent momentum transfer (which is insufficient on its own to reattach the flow under the present conditions, as can be seen from

the baseline results). Similarly, when exploring the influence of Reynolds number, at very low Reynolds number there would be no transition to turbulence, meaning the only active mechanism would be the re-energisation by the secondary flow, while at significantly higher Reynolds number than that considered here, transition would occur closer to the leading edge, and more uniformly across the span. A detailed investigation of these parameters is left as future work.

Some differences are observed between the presently computed lift force and those reported experimentally, although there is sufficient uncertainty in the reproduction of the wind tunnel conditions at this Reynolds number. While it is anticipated there may be sensitivity of the flow to the level of free stream turbulence, we do not include inlet turbulence in these calculations. Despite these differences we anticipate that the insight into the beneficial flow physics induced by the leading edge undulations will hold, although such investigation is left as a future work.

Acknowledgement

Early stages of this work were supported by the UK Turbulence Consortium, funded by the EPSRC under Grant EP/G069581/1, and made use of the facilities of HECToR, the UK's national high-performance computing service.

The work also made use of the facilities of N8 HPC, provided and funded by the N8 consortium and EPSRC (Grant No.EP/K000225/1). The Centre is co-ordinated by the Universities of Leeds and Manchester.

References

[1] Franke E Fish and Juliann M Battle. Hydrodynamic design of the humpback whale flipper. *Journal of Morphology*, 225(1):51–60, 1995.

[2] D. S. Miklosovic, M. M. Murray, L. E. Howle, and F. E. Fish. Leading-edge tubercles delay stall on humpback whale (Megaptera novaeangliae) flippers. *Physics of Fluids*, 16(5):L39, 2004.

[3] H. Johari, C. Henoch, D. Custodio, and a. Levshin. Effects of Leading-Edge Protuberances on Airfoil Performance. *AIAA Journal*, 45(11):2634–2642, November 2007.

[4] K L Hansen, R M Kelso, and B B Dally. Performance Variations of Leading-Edge Tubercles for Distinct Airfoil Profiles. *AIAA Journal*, 49(1):185–194, 2011.

[5] David S. Miklosovic, Mark M. Murray, and Laurens E. Howle. Experimental Evaluation of Sinusoidal Leading Edges. *Journal of Aircraft*, 44(4):1404–1408, July 2007.

[6] Michael Jordan Stanway. *Hydrodynamic effects of leading-edge tubercles on control surfaces and in flapping foil propulsion.* PhD thesis, MIT, 2008.

[7] FE Fish and GV Lauder. Passive and active flow control by swimming fishes and mammals. *Annu. Rev. Fluid Mech.*, 38:193–224, 2006.

[8] Frank E Fish, Paul W Weber, Mark M Murray, and Laurens E Howle. The tubercles on humpback whales' flippers: application of bio-inspired technology. *Integrative and comparative biology*, 51(1):203–13, July 2011.

[9] MM Zhang, GF Wang, and JZ Xu. Aerodynamic control of low-reynolds-number airfoil with leading-edge protuberances. *AIAA Journal*, pages 1–12, 2013.

[10] Ernst van Nierop, Silas Alben, and Michael Brenner. How Bumps on Whale Flippers Delay Stall: An Aerodynamic Model. *Physical Review Letters*, 100(5):1–4, February 2008.

[11] B Thwaites. *Incompressible aerodynamics.* Dover Publications, 1960.

[12] P Watts and FE Fish. The influence of passive, leading edge tubercles on wing performance. In *Proc. Twelfth Intl. Symp. Unmanned Untethered Submers. Technol*. Auton. Undersea Syst. Inst. Durham New Hampshire, 2001.

[13] HS Yoon, PA Hung, JH Jung, and MC Kim. Effect of the wavy leading edge on hydrodynamic characteristics for flow around low aspect ratio wing. *Computers & Fluids*, 49(1):276–289, 2011.

[14] Zhang Xingwei, Zhou Chaoying, Zhang Tao, and Ji Wenying. Numerical study on effect of leading-edge tubercles. *Aircraft Engineering and Aerospace Technology*, 85(4):247–257, 2013.

[15] Paul W Weber, Laurens E Howle, Mark M Murray, and David S Miklosovic. Computational evaluation of the performance of lifting surfaces with leading-edge protuberances. *Journal of Aircraft*, 48(2):591–600, 2011.

[16] Hugo TC Pedro and Marcelo H Kobayashi. Numerical study of stall delay on humpback whale flippers. In *46th AIAA Aerospace Sciences Meeting and Exhibit*, pages 2008–0584, 2008.

[17] Julien Favier, Alfredo Pinelli, and Ugo Piomelli. Control of the separated flow around an airfoil using a wavy leading edge inspired by humpback whale flippers. *Comptes Rendus Mécanique*, 340(1-2):107–114, January 2012.

[18] Joseph Smagorinsky. General circulation experiments with the primitive equations: I. the basic experiment*. *Monthly weather review*, 91(3):99–164, 1963.

[19] Massimo Germano, Ugo Piomelli, Parviz Moin, and William H Cabot. A dynamic subgrid-scale eddy viscosity model. *Physics of Fluids A: Fluid Dynamics*, 3:1760, 1991.

[20] DK Lilly. A proposed modification of the germano subgrid-scale closure method. *Physics of Fluids A: Fluid Dynamics*, 4:633, 1992.

[21] Pierre Sagaut. *Large eddy simulation for incompressible flows*, volume 3. Springer Berlin, 2000.

[22] Raad I Issa. Solution of the implicitly discretised fluid flow equations by operator-splitting. *Journal of Computational physics*, 62(1):40–65, 1986.

[23] Eastman N Jacobs. *The aerodynamic characteristics of eight very thick airfoils from tests in the variable density wind tunnel*. National Advisory Committee for Aeronautics, 1932.

[24] Brian Cabral and Leith Casey Leedom. Imaging vector fields using line integral convolution. In *Proceedings of the 20th annual conference on Computer graphics and interactive techniques*, pages 263–270. ACM, 1993.

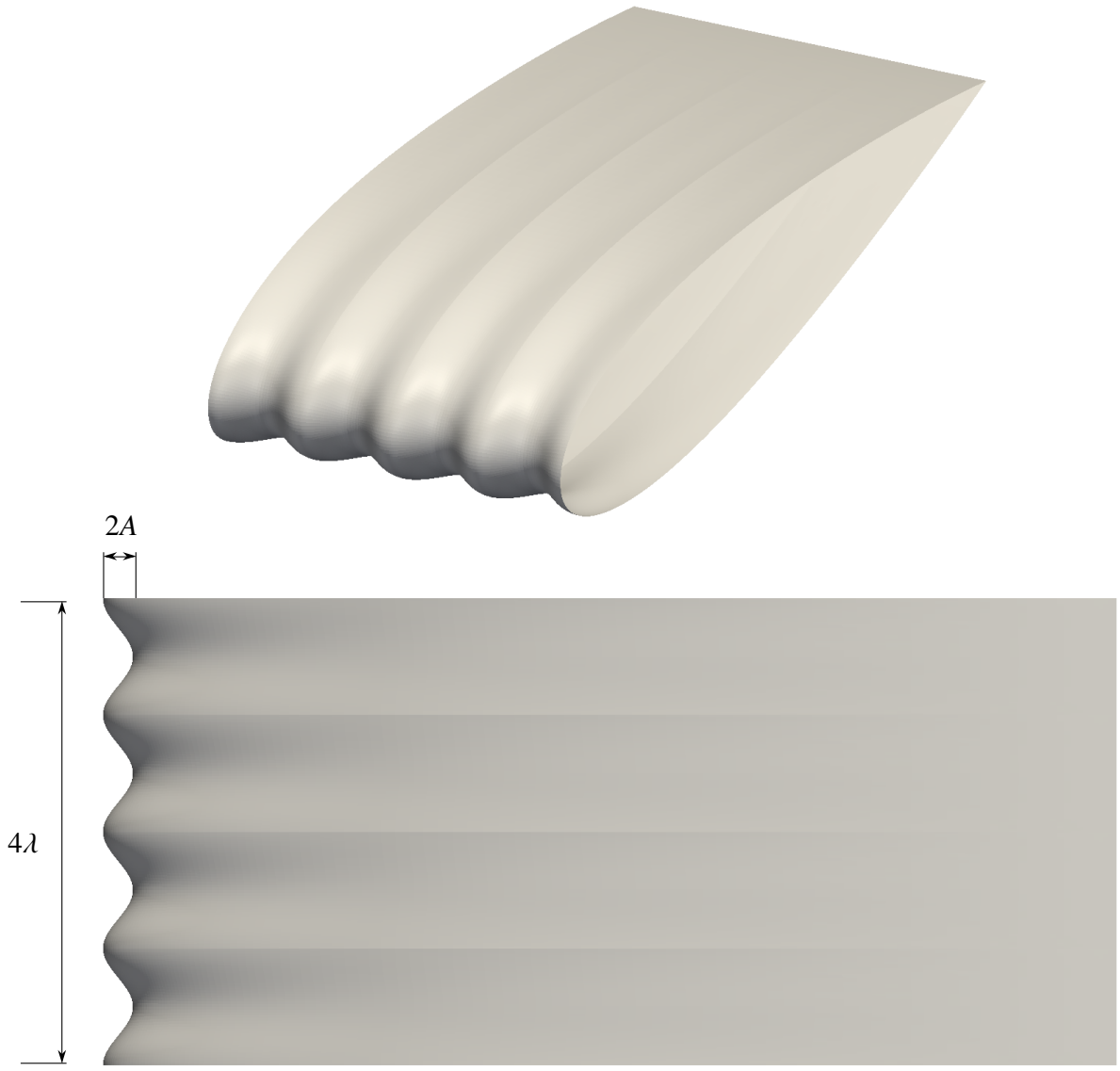

Figure 1. Geometry considered

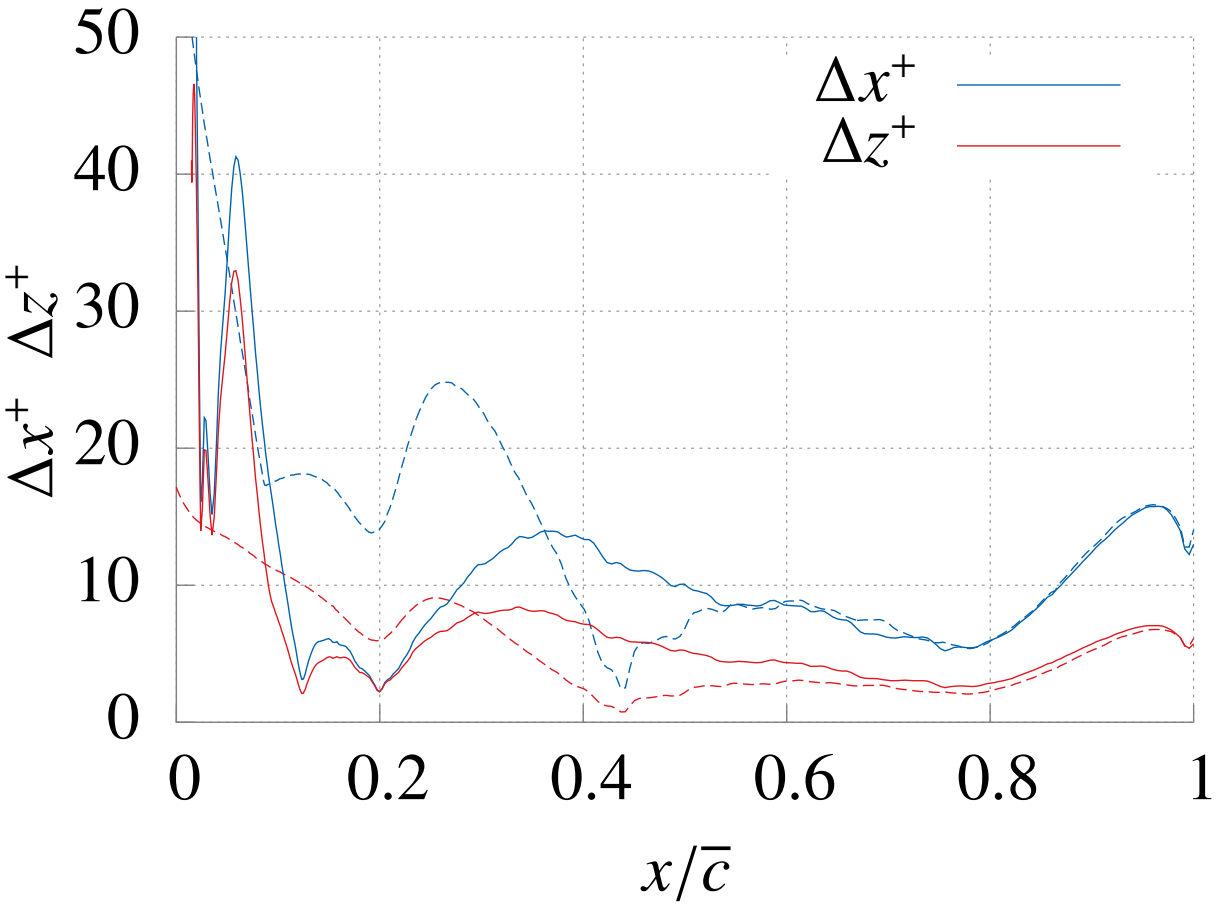

Figure 2. Grid spacing in wall units. Dashed: behind chord maxima; Solid: behind chord minima.

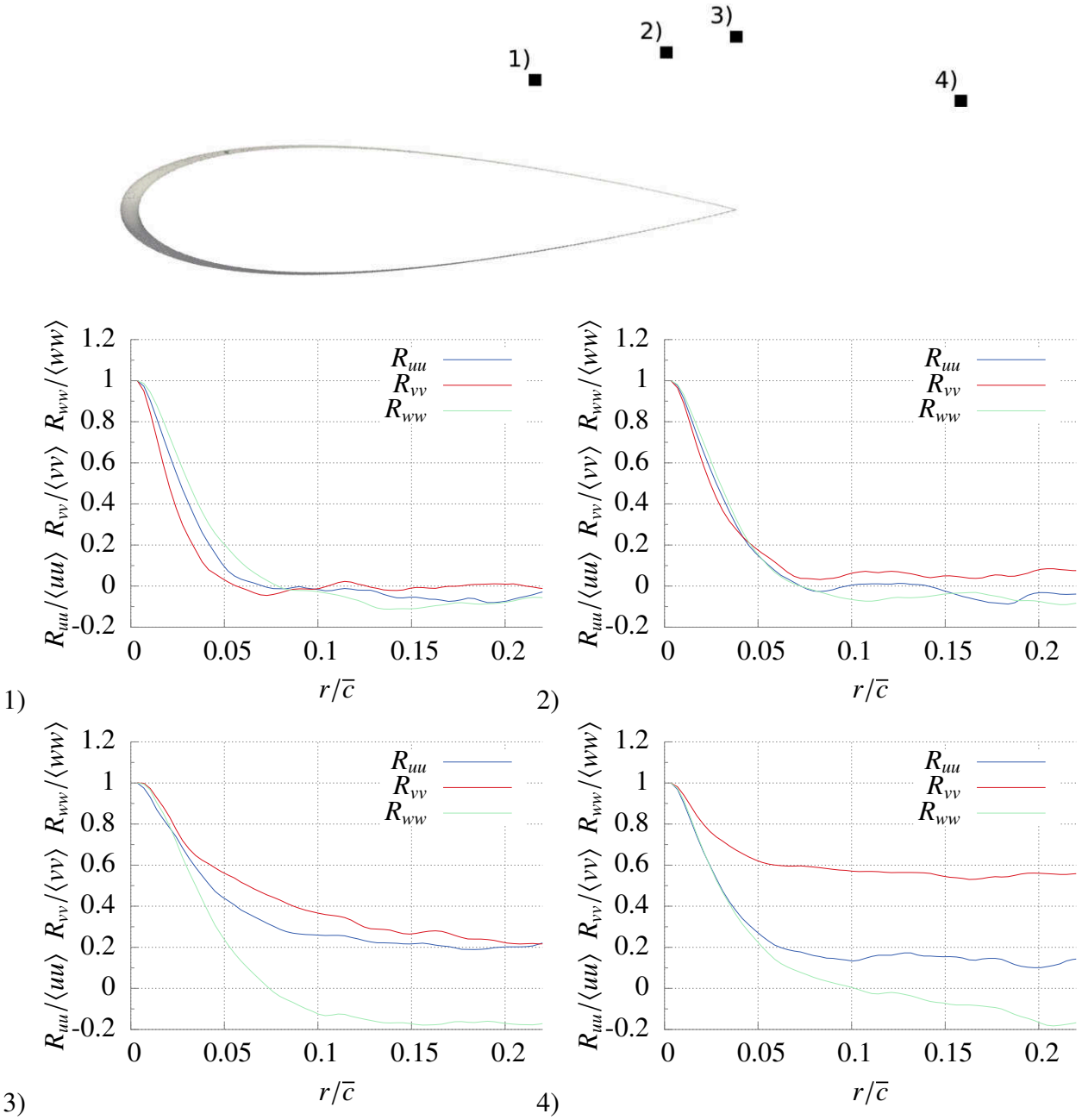

Figure 3. The two-point correlation for the larger span-wise extent simulation. Modified geometry (with undulations). Points taken behind peaks, in the shear layer and wake, as indicated in the top subfigure.

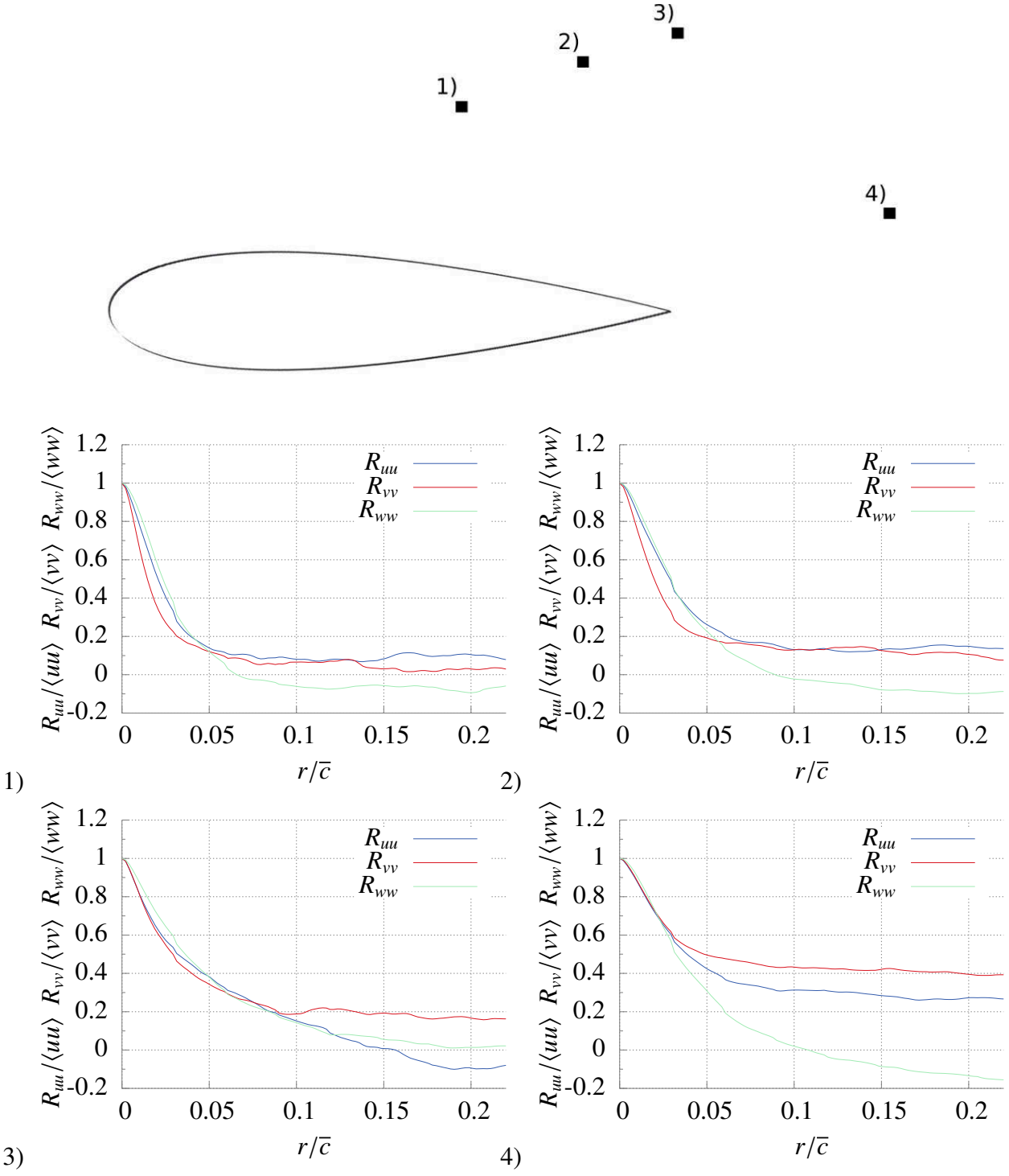

Figure 4. The two-point correlation for the larger span-wise extent simulation. Baseline unmodified geometry (without undulations). Points taken in the shear layer and wake, as indicated in the top subfigure.

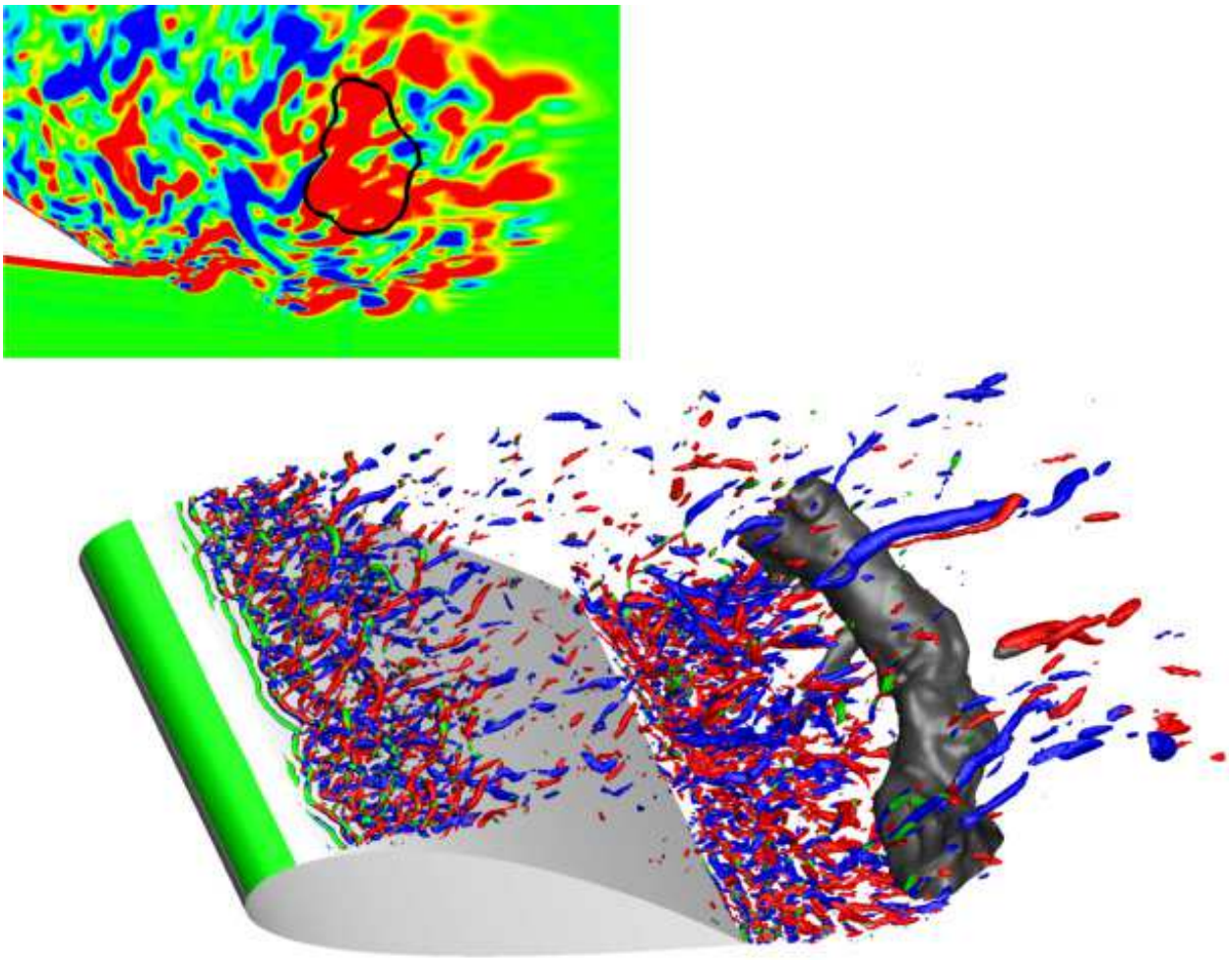

Figure 5. Isosurfaces of $p = -1$, and $Q = 1500$ (coloured by streamwise vorticity, blue negative, red positive) for the unmodified geometry. Inset: contours of spanwise vorticity (levels are between -20 (blue) and +20 (red), and contour of $p = -1$ (solid line)

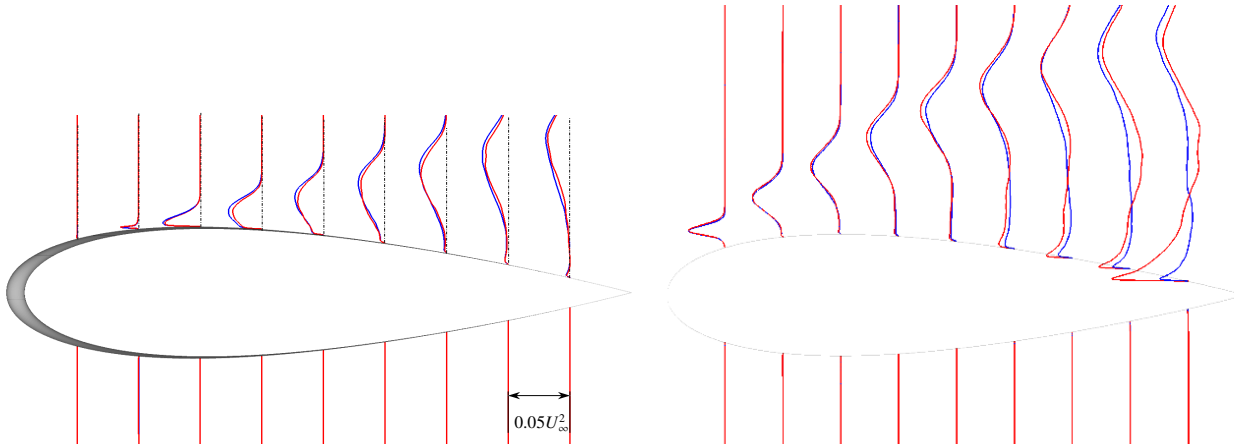

Figure 6. Comparison of time-averaged turbulent shear stress, $\langle uv \rangle$, for simulations with a span-wise extent of 2λ (red) and 4λ (blue). Left: Modified. Right: Baseline. Profiles taken behind peaks for the modified case, and $0.1\overline{c}$ from one another, starting at $x/\overline{c} = 0.1$.

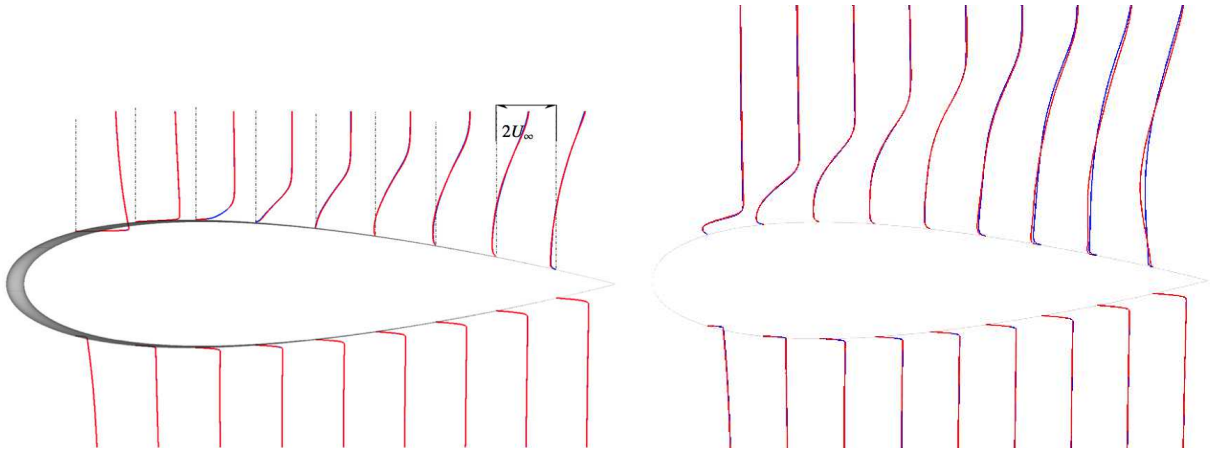

Figure 7. Comparison of time-averaged velocity, $\langle U \rangle$, for simulations with a span-wise extent of 2λ (red) and 4λ (blue). Left: Modified. Right: Baseline. Profiles taken behind peaks for the modified case, and $0.1\overline{c}$ from one another, starting at $x/\overline{c} = 0.1$.

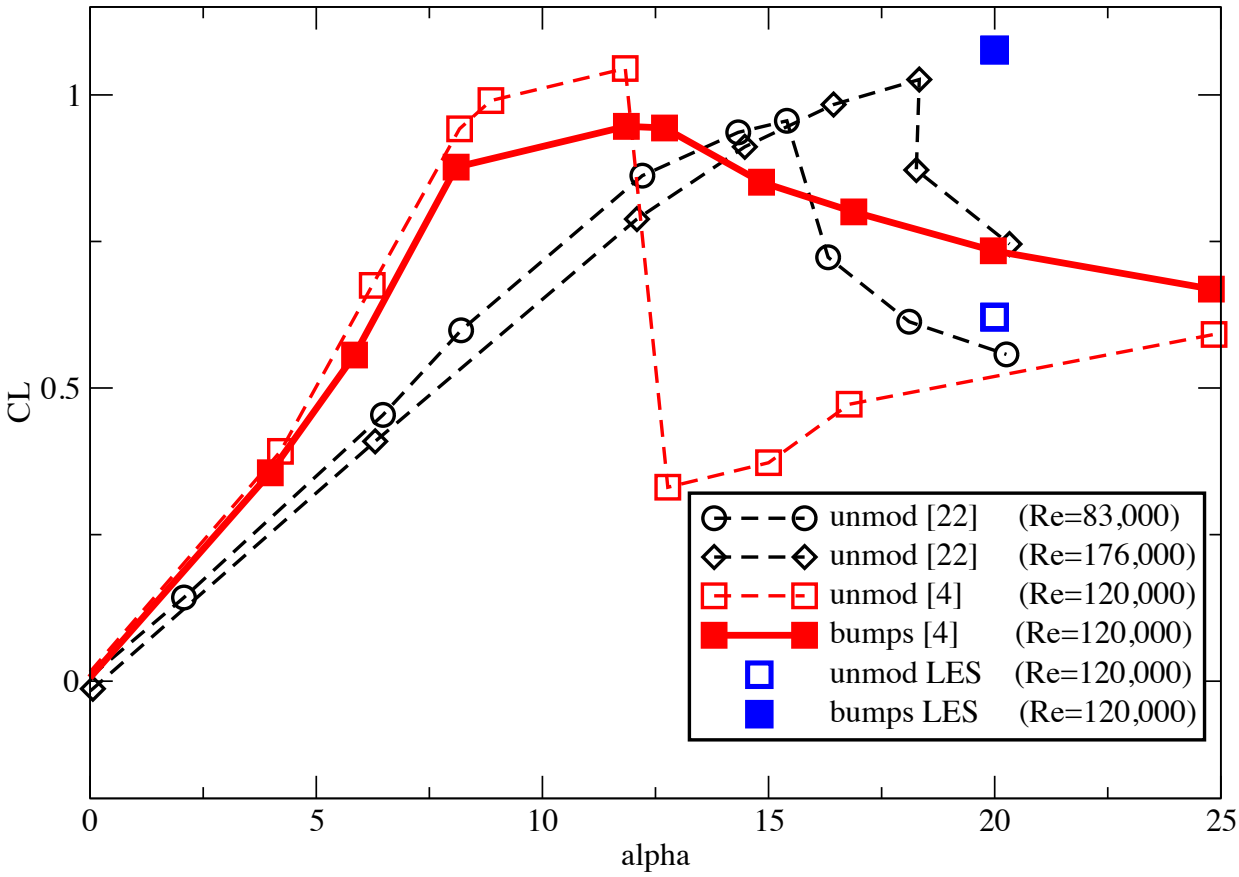

Figure 8. lift comparison with experimental data

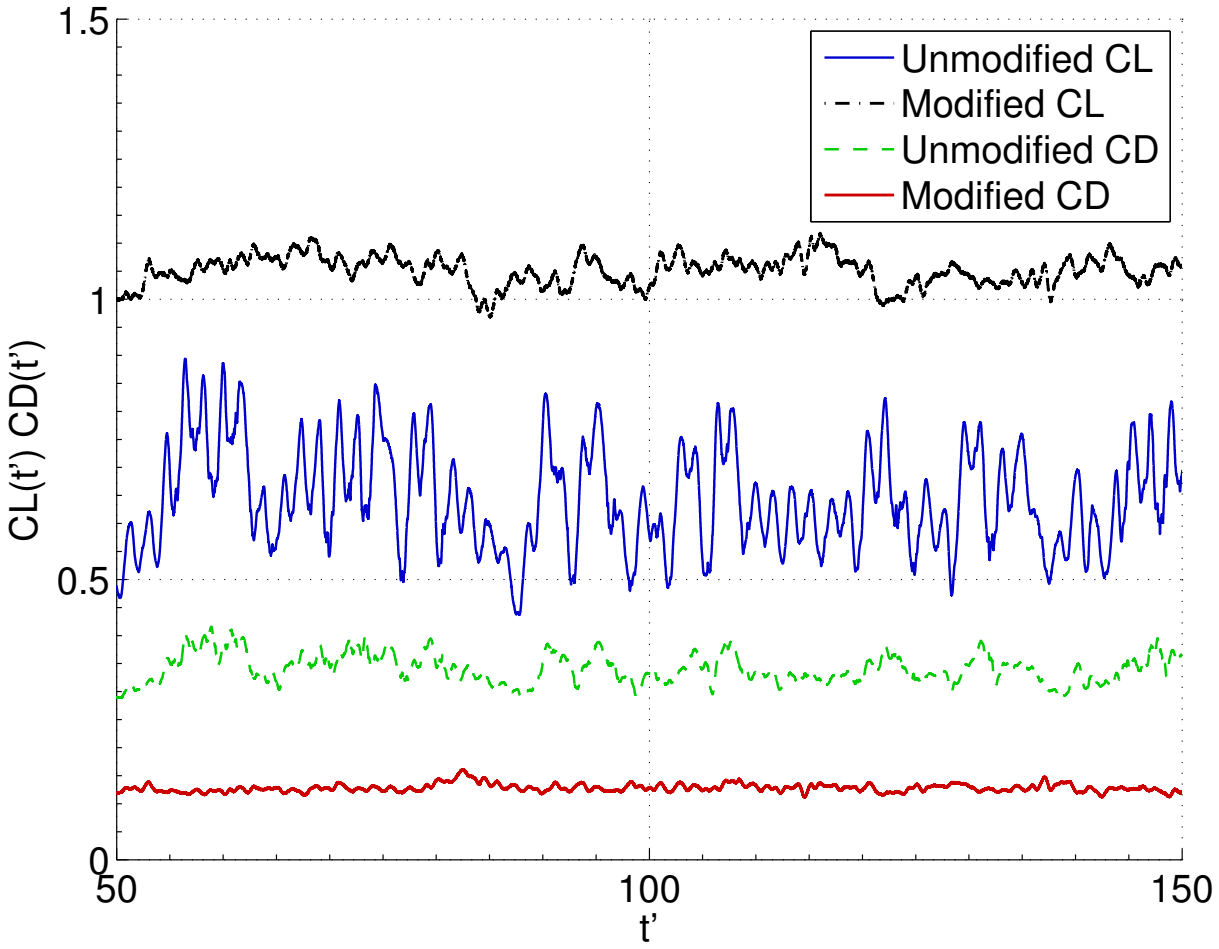

Figure 9. Instantaneous lift and drag coefficients for both modified and unmodified geometries.

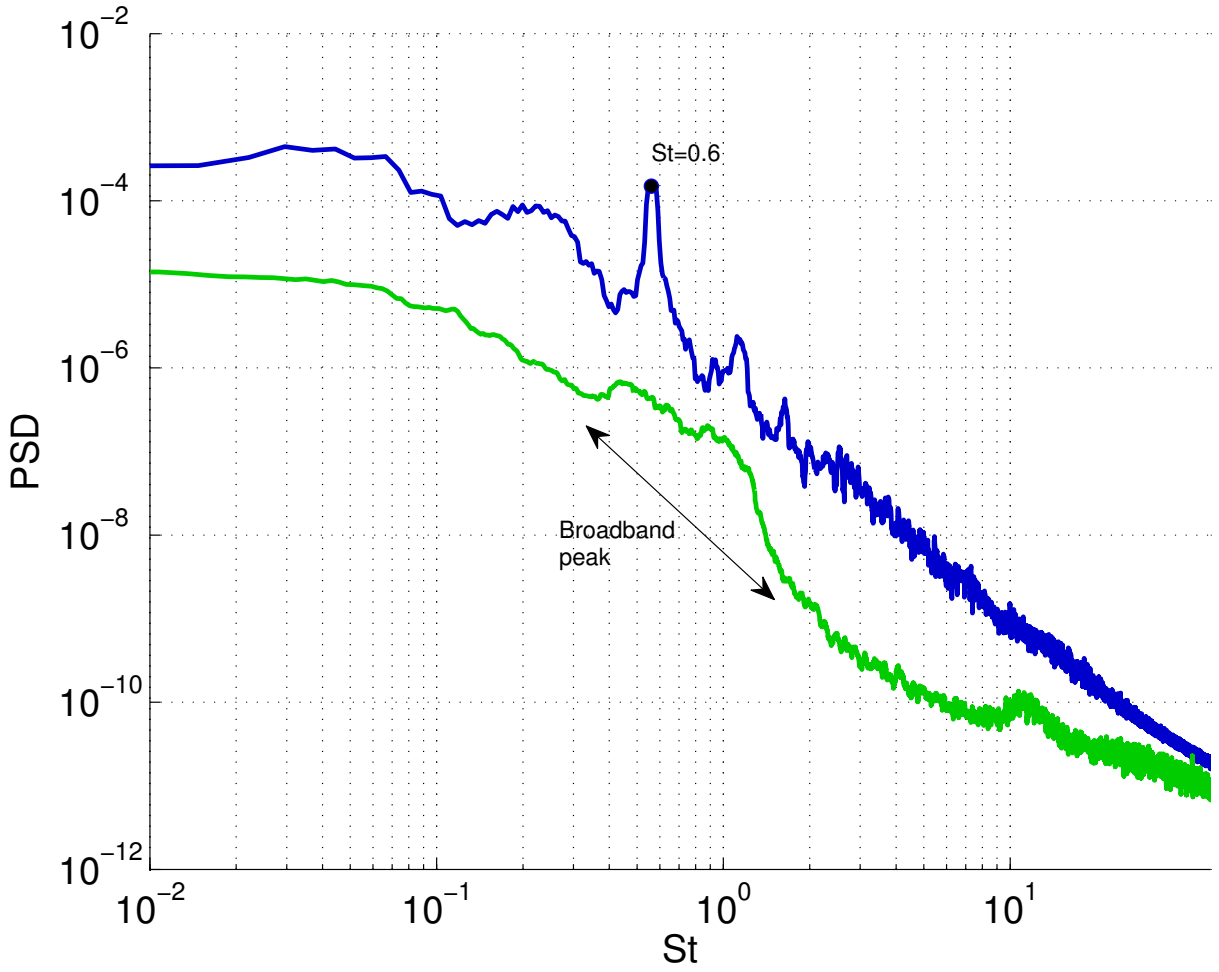

Figure 10. Power spectral density of instantaneous lift for both modified (green) and unmodified (blue) geometries.

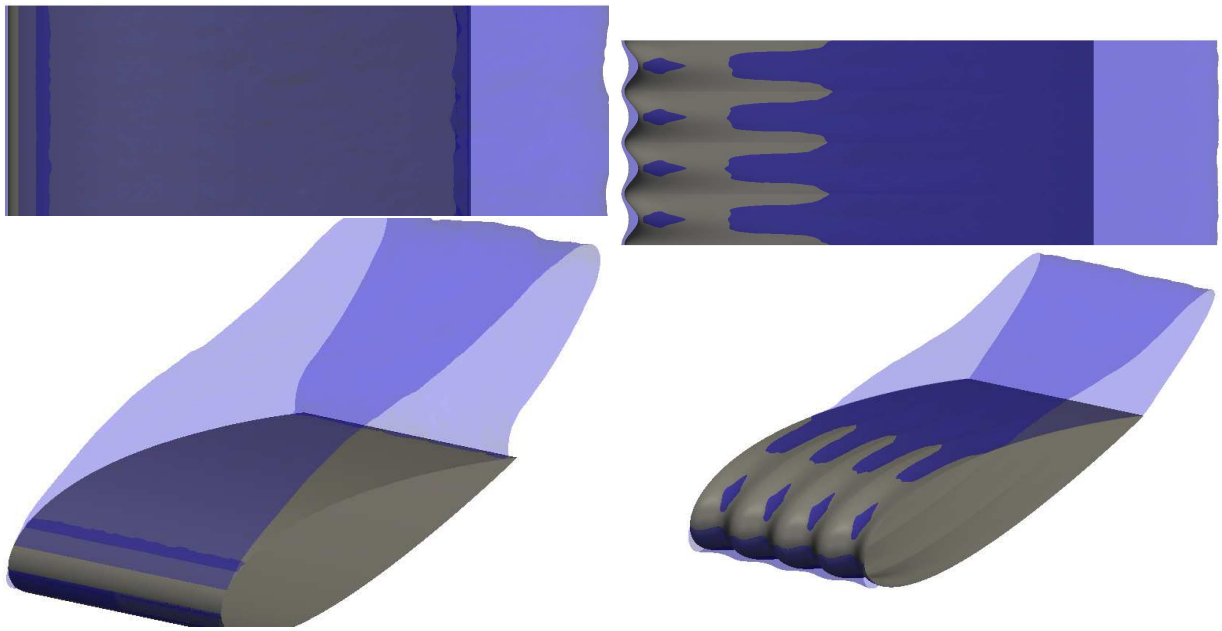

Figure 11. Iso-surface of zero streamwise time-averaged velocity.

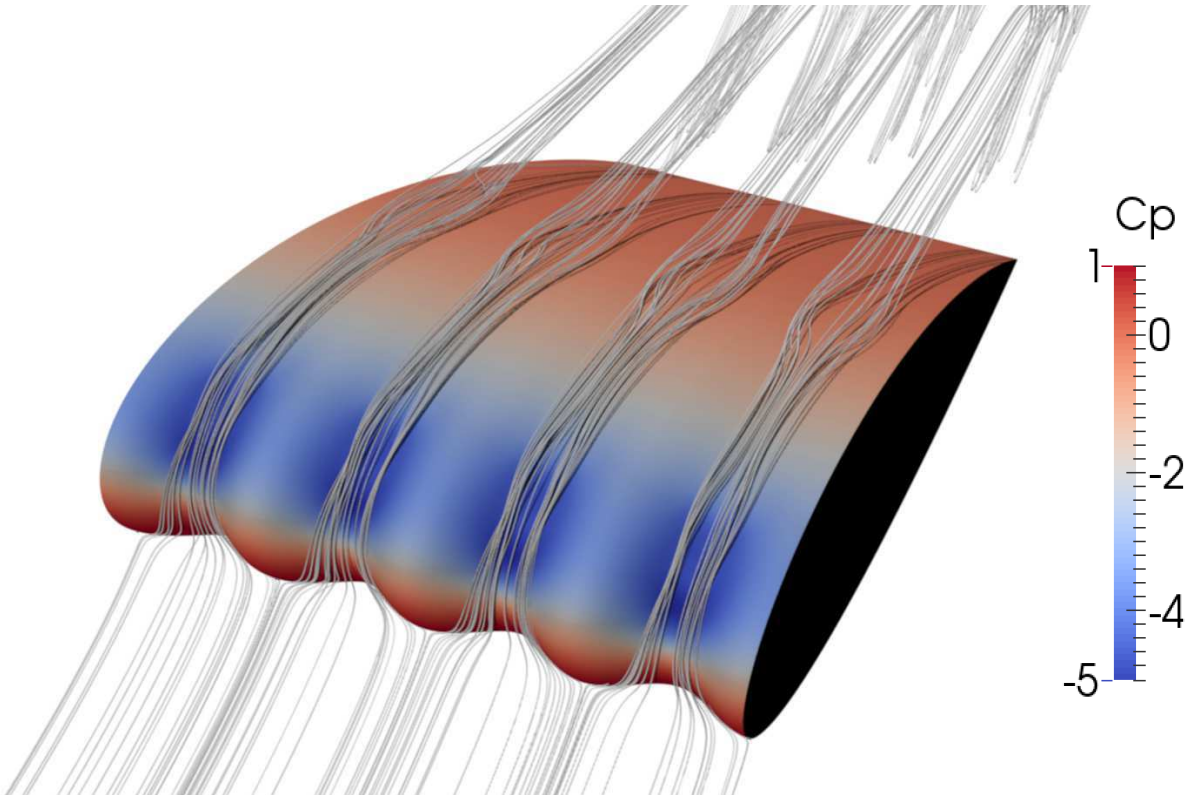

Figure 12. Time-averaged streamlines, showing the deflection of the oncoming flow at the leading edge region. Colour shows pressure coefficient.

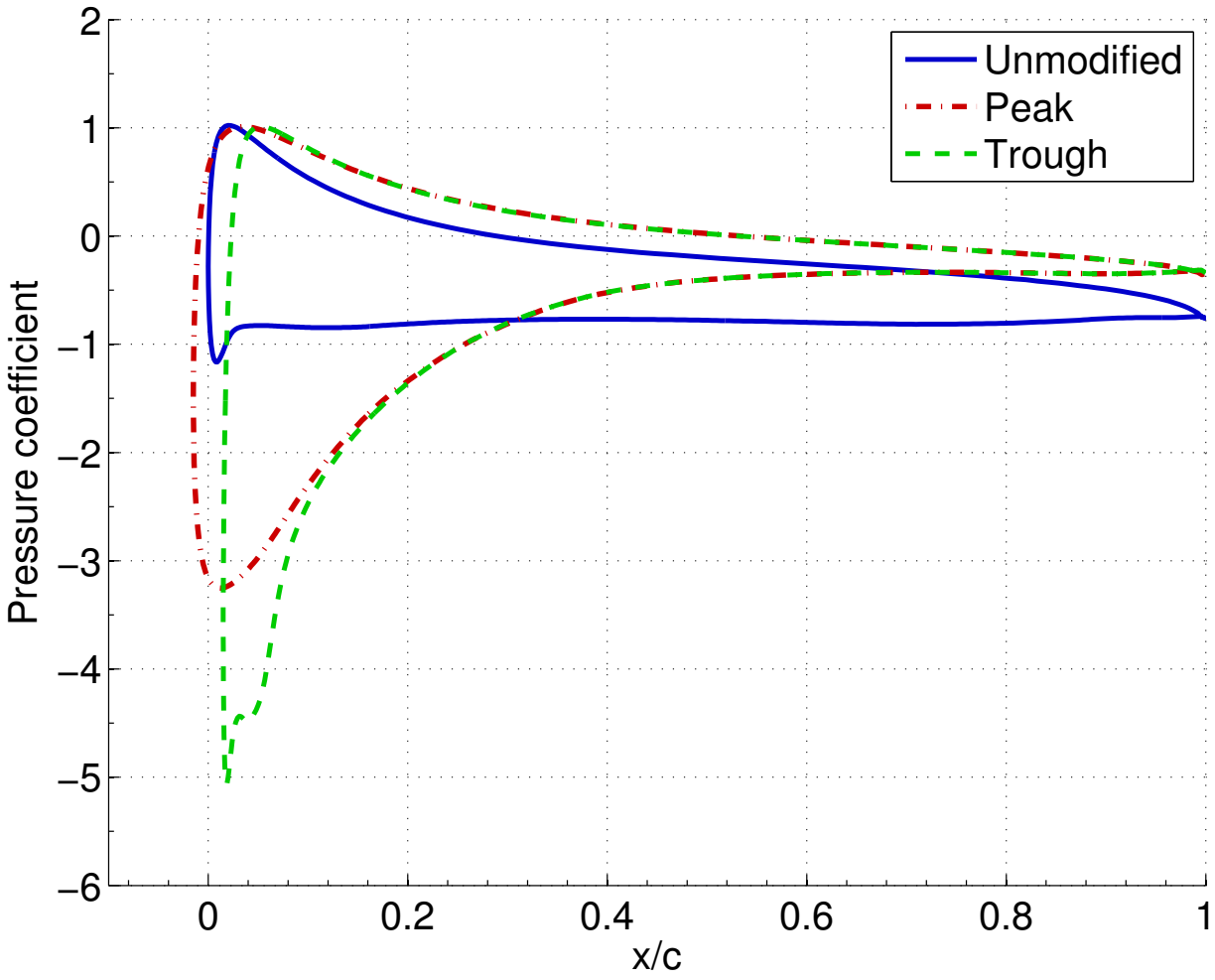

Figure 13. Surface pressure coefficient.

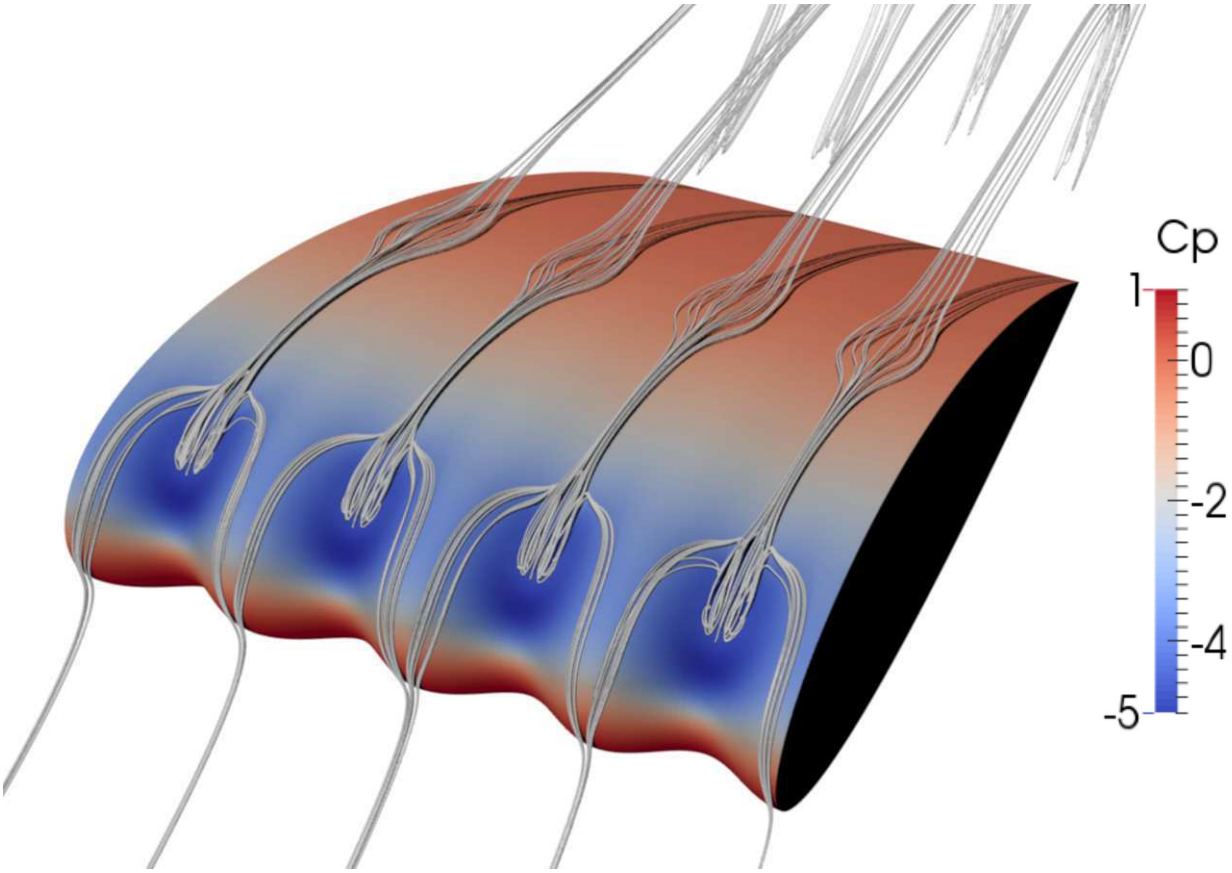

Figure 14. Time-averaged streamlines, showing the secondary flow. Colour shows pressure coefficient.

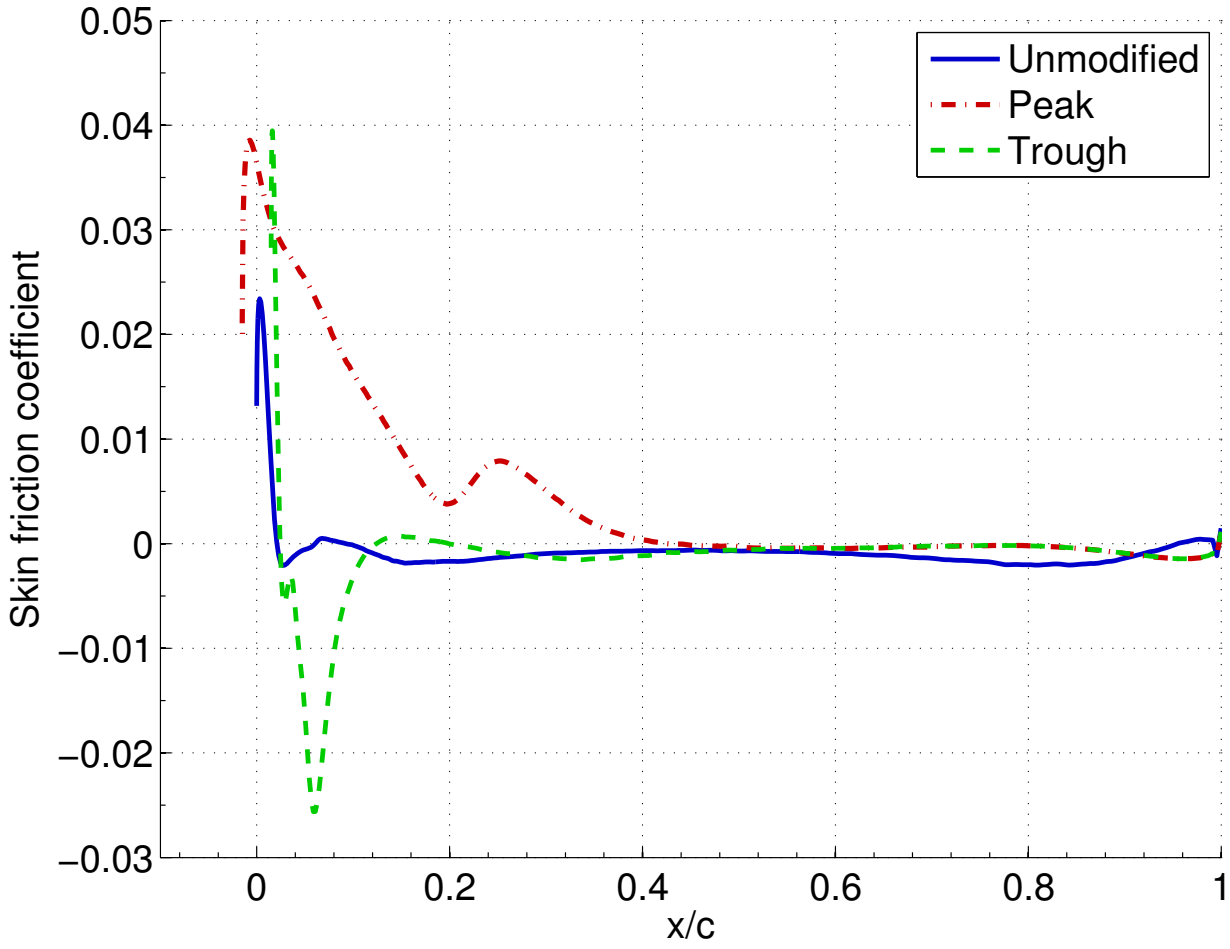

Figure 15. Time-averaged skin friction coefficient.

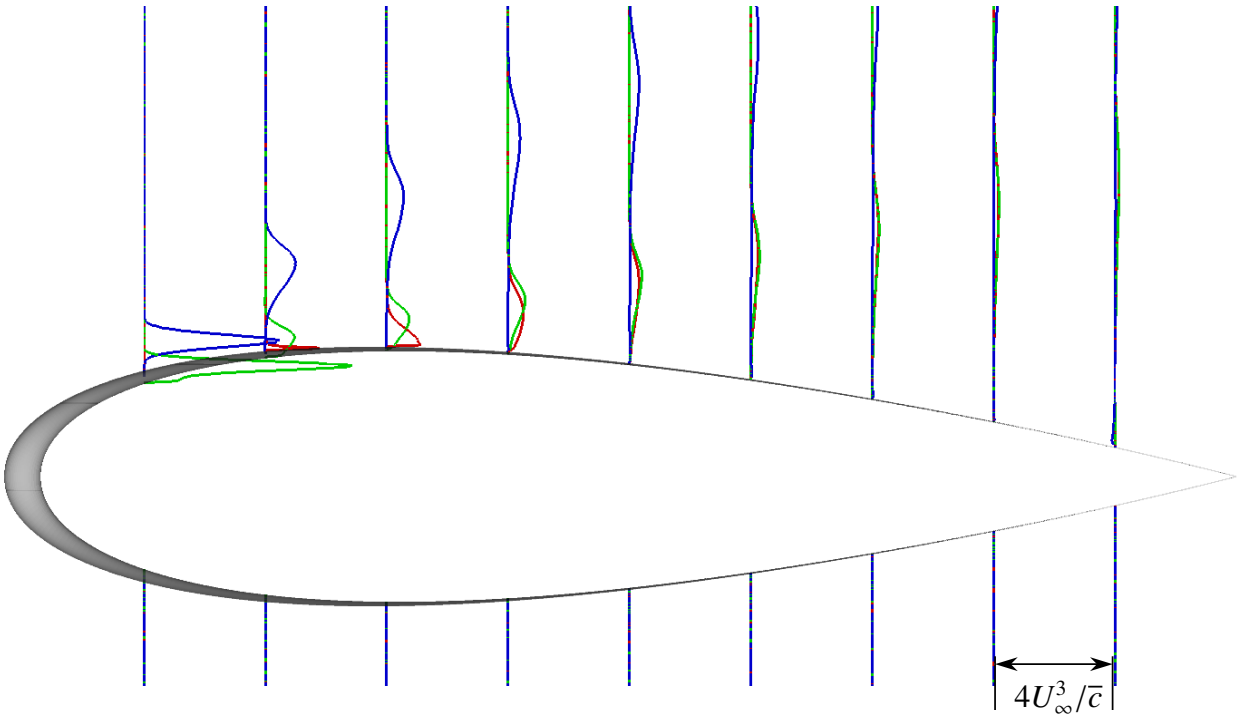

Figure 16. Production term $\mathcal{P} \equiv -\langle u_i' u_j' \rangle \frac{\partial u_i}{\partial x_j}$, taken from budget of turbulent kinetic energy transport equation. Unmodified (blue) behind peak (red) and behind trough (green). Profiles taken $0.1\overline{c}$ from one another, starting at $x/\overline{c} = 0.1$.

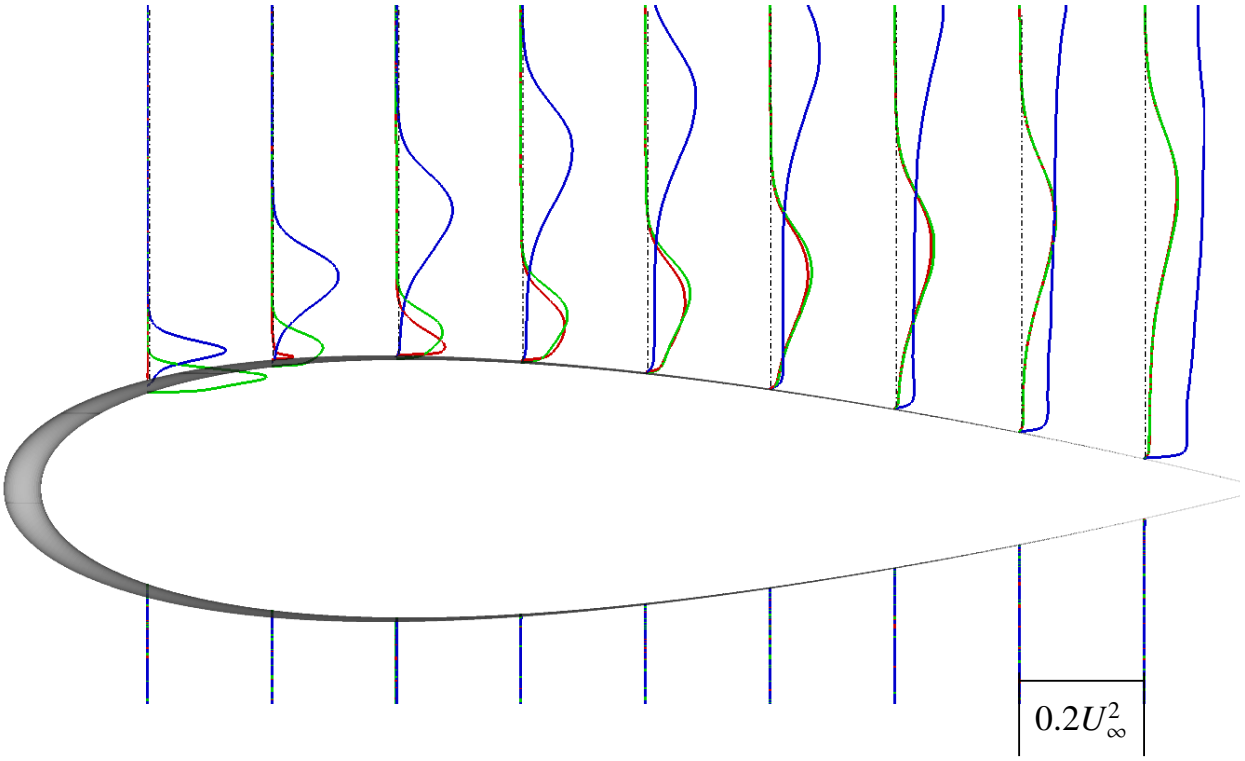

Figure 17. Time-averaged turbulent kinetic energy, k, for unmodified (blue) behind peak (red) and behind trough (green). Profiles taken $0.1\overline{c}$ from one another, starting at $x/\overline{c} = 0.1$.

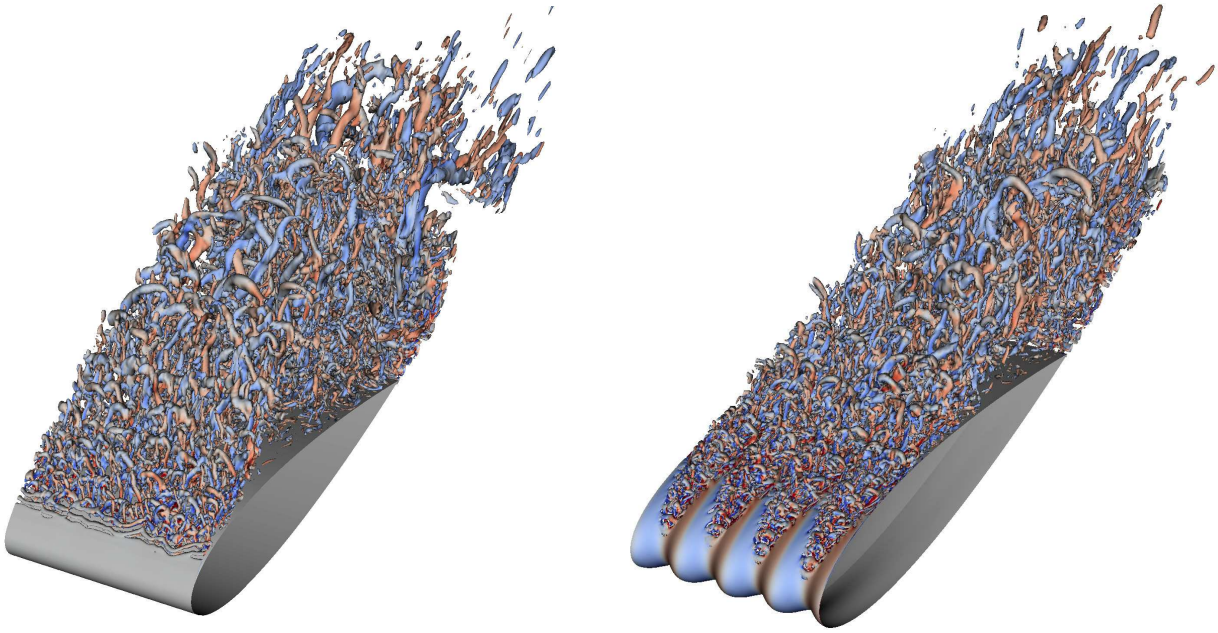

Figure 18. Iso-surfaces of the second invariant of the velocity gradient tensor, $Q = 200$. Left: Unmodified; Right: Modified. Coloured by streamwise vorticity (blue to red).

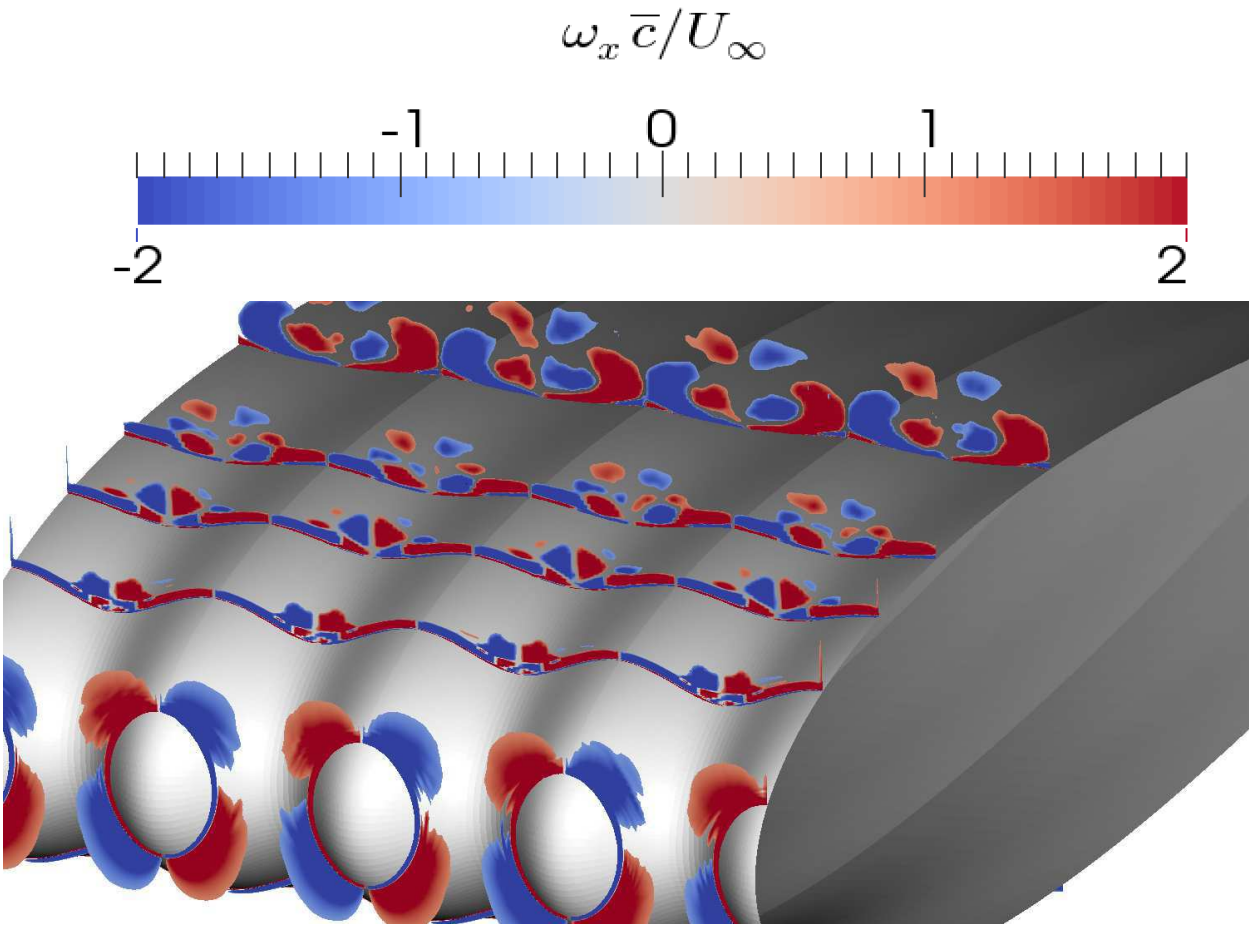

Figure 19. Slices coloured by time-averaged streamwise vorticity.

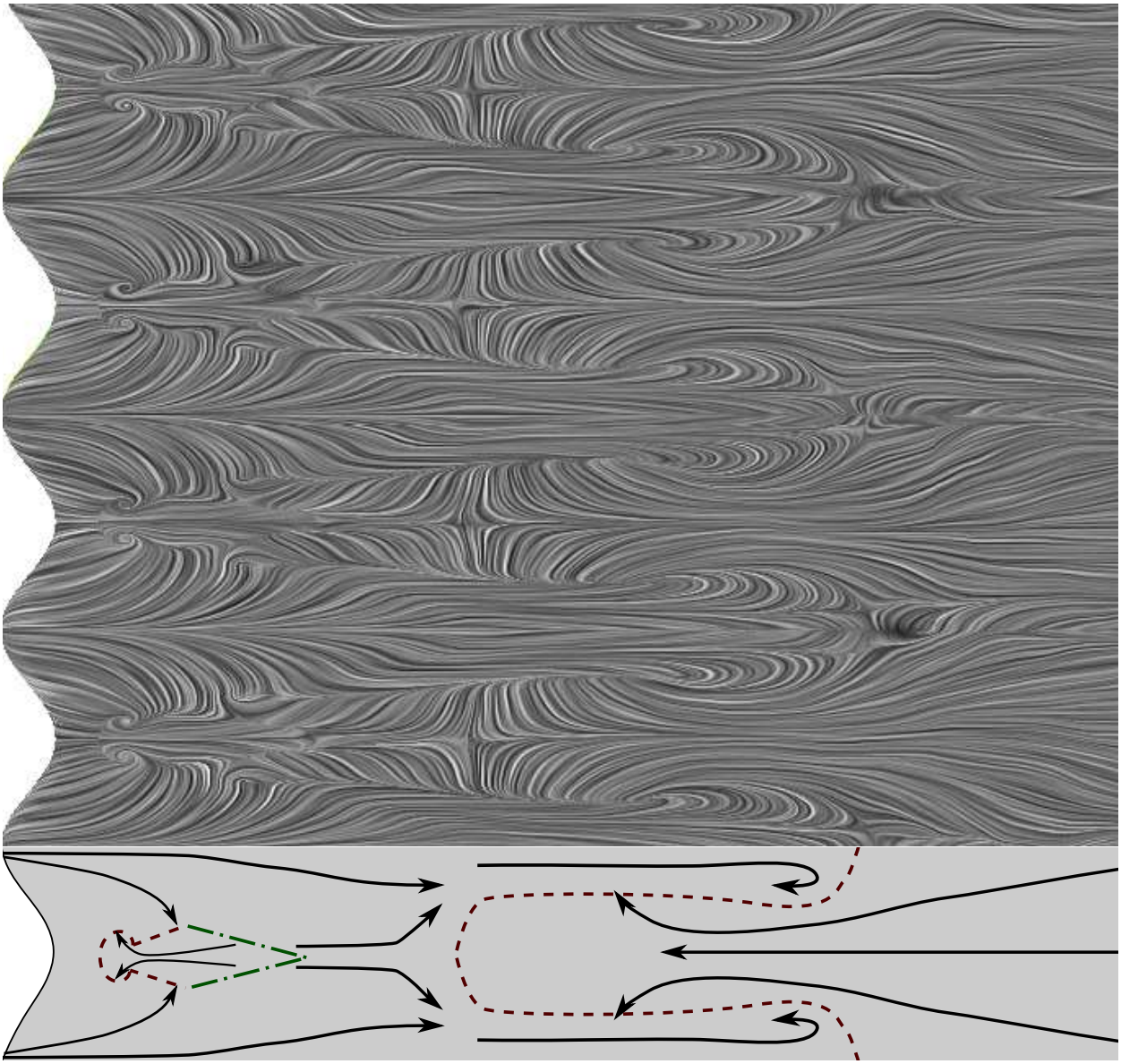

Figure 20. Plot showing time-averaged wall shear stress, visualised with the line integral convolution technique [24] (above) with sketch indicating flow direction (arrows), separation lines (red dashed), and reattachment lines (green dot-dash) (below).